Tribology International 121 (2018) 269–279

Contents lists available at ScienceDirect

Tribology International

journal homepage: www.elsevier.com/locate/triboint

Tilting pad gas bearing induced thermal bow- rotor instability (Morton effect)

Xiaomeng Tong *, Alan Palazzolo

Department of Mechanical Engineering, Texas A&M University, College Station, TX 77840, USA

ARTICLE INFO

Keywords:
Morton effect
Thermal bow
Rotor temperature difference
Tilting pad gas bearing

ABSTRACT

The Morton effect ME is a thermally induced, rotordynamic instability, which is frequently reported in overhung machines supported with oil-lubricated bearings. Synchronous journal whirling results in an uneven viscous shearing of the lubricant film and temperature variation around the journal circumference. This bends the shaft and under certain conditions causes increasing synchronous vibration. Previous research focused solely on oil-lubricated bearings. A transient, high-fidelity ME methodology is presented to expand the scope to tilting pad gas bearing (TPGB) systems. Three dimensional finite element models are established to predict the rotor and bearing temperature and dynamic responses in the time domain. Simulations indicate that the ME can occur in the TPGB systems and may be sensitive to imbalance and overhung mass.

1. Introduction

Gas bearings are widely used in micro-turbomachinery and some of their advantages over other bearing types include low cost, compactness and lightweight. Gas bearings do not require a complicated lubrication circulation system for oil supply or cooling [1,2] as compared with oil-lubricated bearings. In addition, gas bearings are less dependent on costly seals and more environmental friendly being especially suited for oil-free turbomachinery, such as aircraft air cycle machines, turbo-compressors, turbo-generators, etc.

Tilting pad bearings can significantly reduce bearing cross-coupled stiffness by allowing the pad tilting motions to adapt to external load. This aids in avoiding sub-synchronous vibration instability when the rotor is operated over the critical speed. However the pivot, with a typical rocker or spherical geometry may wear, and the resulting increased bearing clearance can dramatically change the bearing behavior, resulting in greater rotor vibration. Flexure pivot tilting pad bearings (FPTPBs) avoid pivot wear by integrating the bearing components into one single piece which is machined with electric discharge machining (EDM) [3–5]. The pad is connected to the bearing through a thin flexure web, and the pad tilting stiffness can be adjusted by changing the web thickness to ensure the suppression of cross coupled stiffness and sub-synchronous instability. The FPTPBs have demonstrated excellent performance in industrial applications and also provide a benefit of eliminating bearing stack-up tolerance.

The increase of the oil, bearing and rotor temperatures due to viscous shearing of the lubricant has always been a design concern. This action decreases lubricant viscosity and also causes bearing and rotor thermal expansions. Accurate prediction of the reduced lubricant viscosity and hot bearing clearance is critical in evaluating the bearing steady performance. This can be achieved by adopting the recent thermo-elasto-hydrodynamic (TEHD) analysis to account for the elastic/thermal deformation of the bearing and rotor on the basis of THD analysis [6–8]. Researchers have found that under certain conditions the Morton effect (ME), which is a thermally induced rotor instability problem, can occur in overhung machines supported by oil film bearings [9–13]. Significant temperature difference (ΔT) may develop across the journal circumference due to synchronous vibration of the journal and the resulting non-uniform viscous shearing of the lubricant. The temperature difference may bend the shaft and induce thermal imbalance. In some cases, the rotor vibration and circumferential ΔT can form a positive feedback, triggering large rotor vibration and ensuing trip of the machinery.

Compared with the oil FPTPBs, the gas FPTPBs generally experience less heat generation due to the lower gas viscosity. However, the advantage of lower viscosity may be lost by the fact that gas bearings typically operate with larger velocity gradient which results from smaller bearing clearances and higher rotating speeds. Thus frictional heating, and the resulting deformations in gas bearings should always be considered. Salehi [14] reported that the maximum bearing temperature could increase by 50°C in a gas foil bearing running at 30,000 rpm.

* Corresponding author.
E-mail addresses: tongxiaomeng1989@tamu.edu (X. Tong), a-palazzolo@tamu.edu (A. Palazzolo).

https://doi.org/10.1016/j.triboint.2018.01.066
Received 7 December 2017; Received in revised form 11 January 2018; Accepted 29 January 2018
Available online 1 February 2018
0301-679X/

Nomenclature

ME	Morton effect
Ω	Rotor spin speed in rad/s
R	Rotor outer radius
h	Film thickness
k	Heat conductivity
C_{pad}	Pad radial clearance
C_{brg}	Bearing radial clearance
h_{sft}	Shaft thermal expansion in radial direction
h_{pad}	Pad thermal expansion in radial direction
T_{pad}	Pad temperature
T_{air}	Air temperature
k_{pad}	Pad thermal conductivity
k_{air}	Air thermal conductively
$M_{rot}, C_{rot}, K_{rot}$	Rotor mass, damping and stiffness matrix
F_{mew2}	Mechanical imbalance force
F_{gyro}	Gyroscopic force
F_{brg}	Bearing force
F_{ext}	External force
$I_\delta, C_\delta, K_\delta, M_{tilt}$	Pad tilting mass, damping, stiffness coefficients and moments
I_p, C_p, K_p, F_p	Pad translation mass, damping, stiffness coefficients and force

Howard [15] found that the gas bearing stiffness decreased with temperature by as much as a factor of two from $25^\circ C$ to $538^\circ C$, indicating that the bearing behavior was heavily temperature dependent. Radil [16] reported thermally induced gas bearing failures including seizure when the bearing was operated with small radial clearance.

Peng and Khonsari [17], Kim and San Andres [18] introduced the THD model to predict the steady state performance of gas foil bearings with improved accuracy relative to isoviscous models. For gas FPTPBs, Sim and Kim [19] presented a TEHD model accounting for the shaft thermal expansion and centrifugal growth. The rotor circumferential temperature distribution was assumed to be uniform so that the circumferential ΔT was always neglected in these previous analyses. This assumption is accurate for bearing steady state analyses such as dynamic coefficient prediction, however, it is not generally valid for ME instability studies, which require more detailed rotor thermal modeling. Prior literature only addressed the ME occurring in overhung machines supported by oil lubricated bearings. The occurrence of the ME in gas bearing machines is becoming of growing importance with increasing industrial applications of gas bearings, especially in turbochargers with overhung masses. The compressibility of the film heightens the level of modeling sophistication needed in prediction models for the ME, especially at the design stage. This paper aims to extend the high-fidelity ME prediction model from oil lubricated bearings to gas bearings, especially gas FPTPBs. The paper's main sections are: Section 2 introduces the theories related to the ME modeling, Section 3 discusses the prediction algorithms, Section 4 verifies the TEHD analysis with measured bearing performance by Ref. [20], Section 5 demonstrates a case study of ME instability in the gas FPTPB system, and Section 6 is the conclusion.

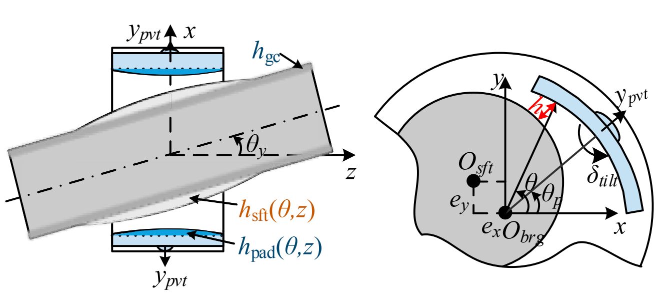

Fig. 1. Film thickness diagram.

2. High fidelity model of gas tilting pad journal bearing

2.1. Reynolds equation

For the ideal gas, the density and pressure are related by $\rho = P/\Re_g T$ with $\Re_g$ and T representing the gas constant and operating temperature, respectively. The Reynolds equation for the ideal gas film is listed in Eq. (1) for the purely hydrodynamic lubrication. The gas viscosity μ is temperature dependent and should be updated at each time step according to the film temperature distribution predicted by the energy equation. Note that x, y, z are the circumferential, radial and axial direction, respectively.

$$\nabla\cdot\left(\frac{-h^3P}{12\mu}\nabla P\right)+\frac{\Omega R}{2}\frac{\partial(Ph)}{\partial x}+\frac{\partial(Ph)}{\partial t}=0 \tag{1}$$

The ambient pressure P_a is imposed on both axial boundaries ($z = 0, L$) of each bearing pad. Distinct from the cavitation model of a fluid film bearing, sub-ambient pressure may exist in the diverging film thickness area of the gas bearing. Hybrid gas bearings operate with both hydrostatic and hydrodynamic lift, the former utilizing externally pressurized gas injected into the bearing through an orifice. The Reynolds equation for the hybrid gas bearing is listed below in Eq. (2) for the orifice area. Note that $\dot{m}_{OR}$ is the mass flow rate through the orifice, A is the effective orifice area πa^2 or πdh, and the mass flow rate $\dot{m}_{OR}$ is detailed in the appendix.

$$\nabla\cdot\left(\frac{-h^3P}{12\mu}\nabla P\right)+\frac{\Omega R}{2}\frac{\partial(Ph)}{\partial x}+\frac{\partial(Ph)}{\partial t}=\frac{\mathscr{R}_g T.\dot{m}_{OR}}{A} \tag{2}$$

2.2. Energy equation

The 3D energy equation takes into account the film temperature in all directions and thus is more precise than the 2D version, which neglects the temperature gradient in the axial direction and may over predict the thermal bow caused by the ME [21]. The 3D energy equation for the gas bearing is shown in Eq. (3), where ρ is the gas density, c_p is the gas specific heat, u, w are the velocity components in the circumferential and axial direction, and μ is the viscosity.

$$\rho c_p\left(\frac{\partial T}{\partial t}+u\frac{\partial T}{\partial x}+w\frac{\partial T}{\partial z}\right)=k\left(\frac{\partial^2 T}{\partial x^2}+\frac{\partial^2 T}{\partial y^2}+\frac{\partial^2 T}{\partial z^2}\right)+\left(u\frac{\partial P}{\partial x}+w\frac{\partial P}{\partial z}\right)+\Phi \tag{3}$$

where, $\Phi=\mu\left[\left(\frac{\partial u}{\partial y}\right)^2+\left(\frac{\partial w}{\partial y}\right)^2\right]$

The velocity field u and w are acquired from the pressure gradient predicted by the Reynolds equation. Note that μ is temperature dependent and thus should be updated accordingly as the temperature field is updated from the energy equation solution. The thermo-viscosity relationship is modeled with a linear function as $\mu(T) = \mu_0 + \alpha T$, where T is temperature in $^\circ C$, $\mu_0 = 1.835 \times 10^{-5} Pa{\cdot}s$, $\alpha = 4E-8$ [14]. Note that the gas viscosity will increase with temperature while the oil viscosity will decrease, and this also contributes to the necessity to perform the thermal analysis for gas bearings at high operating temperature.

2.3. Film thickness formula

During operation, both (1) the rotor centrifugal growth and (2) the thermal growth of the rotor & bearing will reduce the bearing clearance and thus should be included in the film thickness formula. The former is

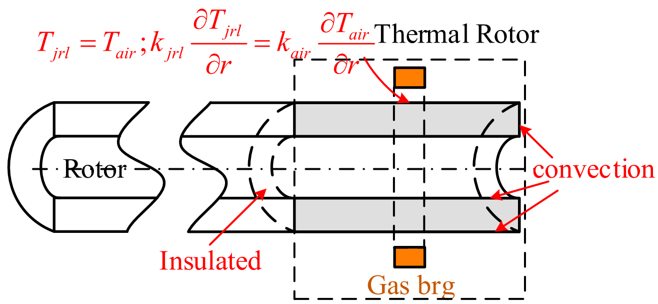

Fig. 2. Thermal boundary condition of the rotor.

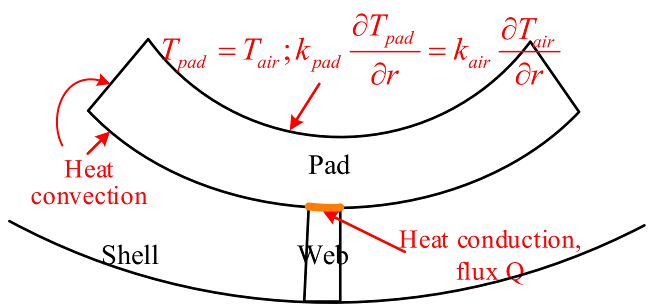

Fig. 3. Thermal boundary condition of the pad.

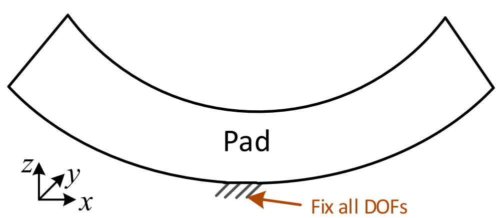

Fig. 4. Thermal deformation boundary condition of bearing.

calculated by Eq. (4) and the latter is detailed in section 2.5.

$$h_{gc} = \frac{\rho_r R \Omega^2}{4E}\left[R^2(1-\nu) + R_i^2(3+\nu)\right] \tag{4}$$

where, R and R_i are the outer and inner radius of the rotor, Ω is the speed rad/s, ρ_r is the rotor mass density, E is the Young's modulus and ν is the Poisson's ratio.

The complete film thickness formula is shown in Eq. (5) and is also illustrated in Fig. 1, where δ_{tilt} is the pad tilting motion and y_{pvt} is the pivot deformation. y_{pvt} can be calculated based on the Hertzian contact theory [22] or assumed to be proportional to the bearing force if the pivot radial stiffness is specified. Note that although the film thickness formula is based on the rigid pad assumption, i.e., the pad is not deformed by the lubricant's pressure, the pad thermal deformation is still included.

$$h(\theta,z) = C_{pad} - \widehat{e}_x\cos(\theta) - \widehat{e}_y\sin(\theta) - \left(C_{pad} - C_{brg}\right)\cos\left(\theta-\theta_p\right) - \delta_{tilt}R\sin\left(\theta-\theta_p\right) - h_{\Delta T}(\theta,z) - h_{gc} \tag{5}$$

where, $\widehat{e}_x = e_x + z\theta_y - y_{pvt}\cos\theta_p$, $\widehat{e}_y = e_y - z\theta_x - y_{pvt}\sin\theta_p$, $h_{\Delta T}(\theta,z) = h_{sft}(\theta,z) + h_{pad}(\theta,z)$

2.4. Thermal model of rotor and bearing

To solve for the rotor and bearing temperature, the transient heat conduction Eq. (6) should be solved and proper thermal boundary conditions should be set up. Note that x, y, z are the circumferential, radial and axial direction, c is the heat capacity, k is the heat conductivity.

$$\frac{\partial^2 T}{\partial x^2} + \frac{\partial^2 T}{\partial y^2} + \frac{\partial^2 T}{\partial z^2} = \frac{\rho c}{k}\frac{\partial T}{\partial t} \tag{6}$$

Considering that the ME instability usually occurs in the rotor non-drive end (NDE), where the overhung mass is typically located, only the NDE of the rotor is detailed for the discussion of thermal boundary conditions. Similar methodologies can be easily extended to the rotor drive end (DE) if necessary. As illustrated in Fig. 2, the rotor section close to the gas bearing location is called "thermal rotor" since it experiences a bearing related temperature increase, and thus its temperature and thermal deformation should be carefully considered. The temperature of the rotor further away from the bearing may be unaffected by bearing heating and will not contribute to the thermal bow. In the current analysis, the "thermal rotor" length is set to be seven times of the bearing width to sufficiently balance desired accuracy and computational cost according to early studies [11,23,24]. The rotor surfaces exposed to ambient air are prescribed with heat convection boundary conditions, including the rotor outer and inner circumference as well as the rotor right end. The left thermal rotor end is imposed with an insulated boundary condition to express an assumed temperature uniformity far

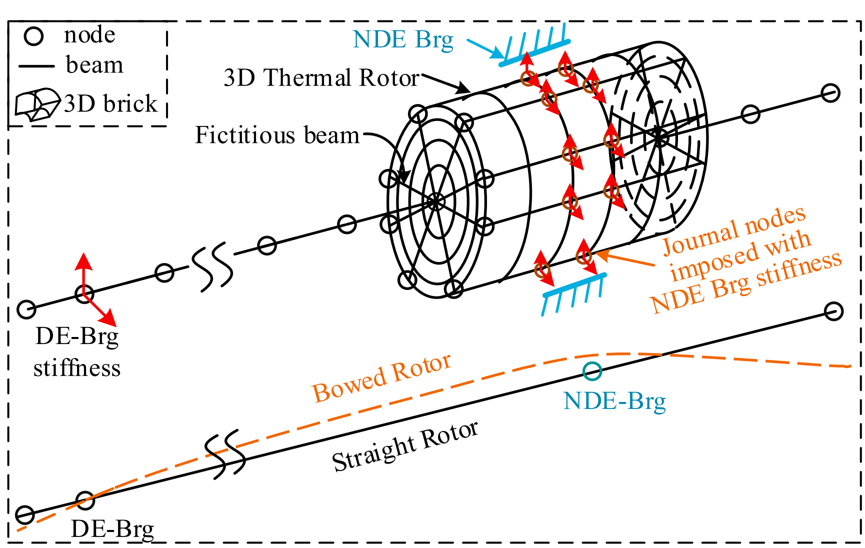

Fig. 5. Hybrid beam – solid element finite element model for thermal bow prediction.

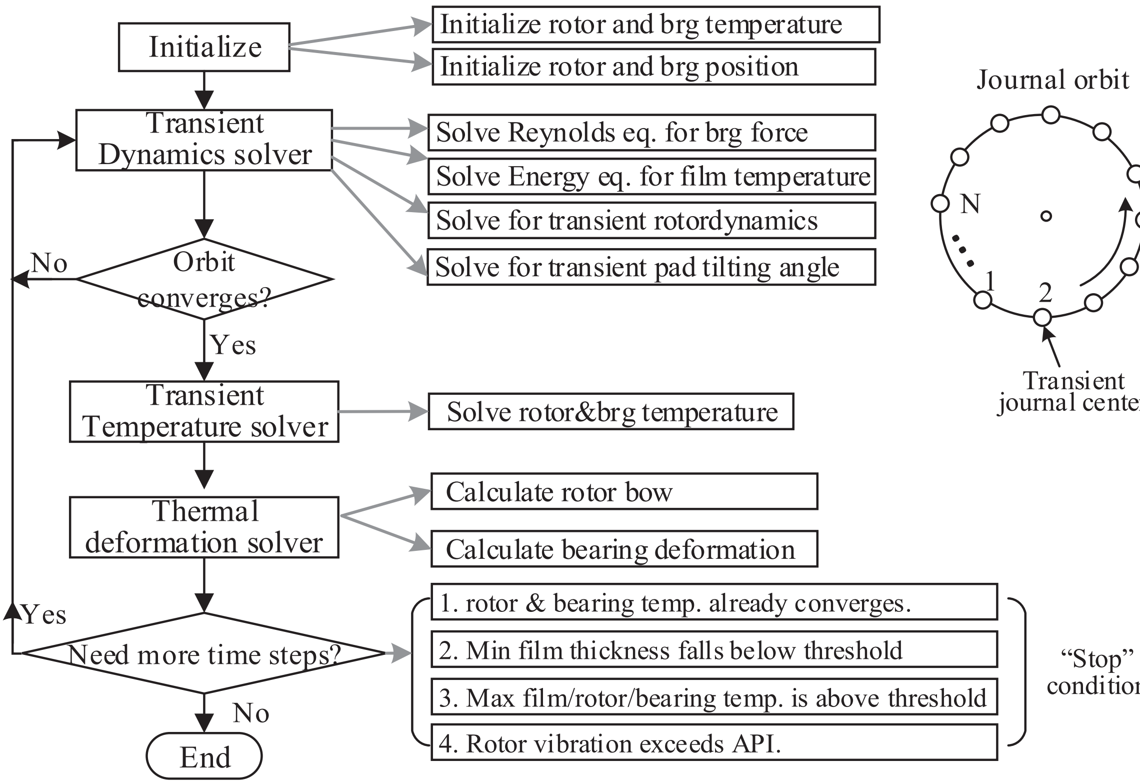

Fig. 6. Morton effect prediction algorithm for gas bearing supported shafts.

from the bearing. At the journal/lubricant interface, continuity of temperature T and heat flux $k\frac{\partial T}{\partial r}$ are imposed.

The thermal boundary condition of the bearing pad is shown below in Fig. 3. Note that at the pad inner surface, i.e., pad-film interface, both the temperature and heat flux are set to be continuous. All pad surfaces exposed to ambient air are prescribed with heat convection. The heat conduction flux Q at the web has the simplified form $Q = c_w\cdot(T_{pad} - T_{shell})\cdot A$, where A is the web cross-section area, c_w is the linear coefficient and is determined from the bearing material and geometry. An estimate of c_w can be determined from finite element modeling at the beginning of ME analysis, and in the following discussion $c_w = 6.5E3\ W/m^{2\circ}C$, which is consistent with [19] due to similar geometries.

2.5. Thermal deformation of the rotor and bearing

The thermal deformations of the bearing and rotor are obtained by solving the 3D finite element model stiffness relation Eq. (7). In this equation $X_{\Delta T}$ is the vector of x, y, z direction nodal displacements, and $F_{\Delta T}$ is the thermal load vector due to the bearing heating related to rotor and bearing temperature distributions. The web thermal deformation is assumed to be negligible due to its relatively smaller dimension and lower temperature increase compared with the pad. As shown in Fig. 4, the web is fixed with all degrees of freedom (DOFs) in the thermal deformation finite element model. The pad will thermally expand inwards, resulting in the clearance reduction. Note that for the dynamics model discussed in section 2.6, the pad is of course free to tilt and move radially, constrained only by the tilting and pivot stiffness.

$$[K_{\Delta T}][X_{\Delta T}] = [F_{\Delta T}] \tag{7}$$

A hybrid beam – solid finite element model (HFEM) [12] is used to predict the rotor thermal bow, where the thermal rotor, which experiences bearing heating related temperature increase, is modeled with 3D brick elements and remaining rotor sections are modeled with beam elements, as illustrated in Fig. 5. The HFEM accelerates the prediction compared with a fully 3D solid element model, without sacrificing accuracy, considering that the non-thermal rotor sections experience negligible temperature increase. Fictitious beams are added at both side surfaces of the thermal rotor to transmit the thermal bending moment from the 3D brick elements to the beam elements. The NDE gas bearing stiffness is imposed by distributing the resulting force in an averaged manner over the journal nodes, while the stiffness of DE bearing is imposed on the beam node, accordingly. Rindi et al. [25] also adopted a similar HFEM, where tetrahedral elements were employed instead of brick elements in order to benefit from automated meshing software for complex geometries. The brick elements provide better computational efficiency but require a more challenging meshing task. Fig. 5 also shows a bowed rotor profile overlaid on the original straight rotor. Note that the thermal deformation of the rotor also expands the rotor radius by h_{sft} in addition to causing the thermal bow, and the h_{sft} together with the pad expansion h_{pad} is fedback to Eq. (5) to update the film thickness. In the current analysis, only the NDE rotor-bearing is analyzed for the ME, nevertheless, the methodology can be conveniently extended to both rotor sides.

2.6. Dynamic model of rotor and bearing

The governing equation for the rotordynamic model, including the ME, is shown in Eq. (8). The thermal bow vector is U_{bow}, where for the ith node along the rotor, $U^i_{bow} = [x^i, \theta^i_x, y^i, \theta^i_y]$. The bearing force F_{brg} is determined by solving the Reynolds equation at each time step, instead of employing linearized force bearing dynamic coefficients. The latter approach was reported to compromise prediction accuracy as the journal center moves significantly away from its equilibrium position [11]. In earlier studies, the rotor thermal bow effect was modeled as an equivalent "thermal imbalance", which was the product of the lumped mass and thermal deflection at the overhung node [11,21,26,27]. This approximation neglects thermal bending moments and may inaccurately predict the ME instability onset speed [12]. The present approach adopts the bowed rotor method in Eq. (8), which can also be extended to other non-thermal bow cases (i.e., permanent bow caused by manufacture error, gravity sag, assembly tolerance, etc.). The concept of thermal imbalance is included in this paper only for purposes of intuitively explaining the development of the ME, not for dynamics prediction.

$$[M_{\text{rot}}]\left[\ddot{U}\right]+[C_{\text{rot}}]\left[\dot{U}\right]+[K_{\text{rot}}][U-U_{\text{bow}}]=\left[F_{\text{mew2}}+F_{\text{gyro}}+F_{\text{brg}}+F_{\text{ext}}\right] \quad (8)$$

The pad dynamics model in the current analysis assumes that the pad acts as a rigid body described by 2° of freedom DOF, i.e., pad tilting δ_{tilt} and pivot deformation y_{pvt}. Tong and Palazzolo [28] utilized a fully flexible pad dynamics model for ME analysis with oil-bearings. The case study with rigid/flexible pad models showed that the pivot flexibility typically dominated the pad flexibility for influence on rotordynamics, and the rigid-pad-flexible-pivot model was a good approximation in most cases. The current analysis therefore still adopts the rigid pad assumption for the gas FPTPBs, since the unit load for gas bearings is generally much lower than for oil bearings. However, a future research study will provide a more comprehensive analysis of pad flexibility's influence on ME in gas FPTPBs.

The governing equations of the pad dynamics are listed in Eq. (9) and Eq. (10). In the current analysis, the pad's internal damping C_δ and C_p are neglected, being much smaller than the damping exerted by the fluid film. The tilting moments M_{tilt} and pivot force F_p come from the integration of bearing film pressure by the Reynolds equation.

$$I_\delta\ddot{\delta}_{tilt}+C_\delta\dot{\delta}_{tilt}+K_\delta\delta_{tilt}=M_{tilt} \quad (9)$$

$$M_p\ddot{y}_{pvt}+C_p\dot{y}_{pvt}+K_p y_{pvt}=F_p \quad (10)$$

3. Prediction algorithm of Morton effect

The flow diagram steps for ME prediction, is illustrated in Fig. 6, and includes: (1) the algorithm initializes the rotor and bearing position and temperature from user-defined files. (2) The software then executes the transient dynamic solver according to Eq. (8) ~ Eq. (10) by numerical integration to predict the rotor and pad dynamics until convergence. Note that each synchronous rotor orbit is divided into N segments both spatially and temporally, and the gas film temperature field is determined at the end of each segment and then is orbit-averaged to get the temperature and flux at the bearing/film and journal/film interfaces. The temperature and flux are imposed in the thermal solver to update the rotor and bearing temperatures. The orbit averaging process of the film temperature is performed in the shaft rotating frame when updating the film/journal boundary condition, i.e., at the time instant t_0, $\theta=\theta_0$ in the rotating frame corresponds to the angle $\theta=\theta_0+\Omega t_0$ in the film - stationary frame. (3) The rotor and bearing transient temperatures are predicted based on the updated thermal boundary conditions. (4) The rotor thermal bow and bearing thermal deformation are predicted at the end of the temperature solver according to Eq. (7) and the HFEM, and then fedback into the dynamic solver to prepare for the next iteration. This transient algorithm will continue until one of the "stop" criteria is met such as abnormal temperature, large vibration or low film thickness (indicating severe ME instability). API [29] refers to the American Petroleum Institute's, or other organization's limits for allowable vibration amplitude of the journal. The transient algorithm will also be terminated after it detects the convergence of rotor vibration and temperature, if the system is ME stable.

The rotordynamics and thermodynamics change continuously with time, the former with a very short time constant and the latter with a much longer time constant for the journal and bearings. This results in the conflicting simulation requirements of a long simulation time with a very small integration time step. A staggered, numerical integration scheme is employed to balance these requirements in a computationally practical manner. In Step 2, the transient structural dynamics system is numerically integrated within duration $t1$ by assuming that the rotor and bearing temperature is not changing during this period; In Step 3, likewise, the temperature solver is integrated within duration $t2$ assuming that the dynamics are unchanging. Considering that both $t1$ and $t2$ are small (from several milliseconds to 1 s), the staggered solution will satisfy most engineering applications. Moreover, since the heat transfer processes develop much slower than the rotordynamics, $t2$ is usually set larger than $t1$ to speed up the simulation process without overly compromising accuracy.

A large portion of the computational effort results from the 3D film temperature predictions for dozens of orbit segments with the current algorithm. The effort is amplified by the fact that the shaft thermal boundary condition has to be acquired by orbit-averaging the film temperature. Rindi et al. [25] proposed reducing the computational time required for the transient ME analysis by integrating experimental results into the model, specifically the shaft temperature distribution including the journal ΔT and the hot spot position (with the highest temperature). This is a sound approach, but may require a large test matrix and extensive hardware components with varied design variables, such as, oil viscosity, bearing configuration, orbit size and rotating speed, etc.

4. Verification with bearing static performance prediction

Similar ME methodologies have been successfully applied and verified with both experiments measuring journal ΔT [30], and simulation studies [12] predicting instability onset speed. The present gas bearing ME approach was benchmarked with steady state performance cases appearing in the literature since to the best of the author's knowledge no prior gas bearing ME papers exist. A justification for this approach is that if the rotor thermal bow is set to be zero or the rotor is assumed to be circumferentially isothermal, the ME prediction approach reduces to a general TEHD analysis. Thus the published experimental and TEHD predictions for gas bearing steady state performance, such as for eccentricity, dynamic coefficients, etc., provides the best means for benchmarking the gas baring ME model. However future measurements of rotor circumferential temperature for gas bearings will ultimately provide the best benchmark for prediction methods.

The linear bearing coefficient prediction process requires three steps: (1) predict the bearing & journal steady state temperature and position, (2) calculate the full coefficient matrix by the linear perturbation method with each matrix element acquired by $k=\Delta F/\Delta s$, where Δs is the perturbation of certain DOF, such as tilting angle, pivot displacement, and journal position, ΔF is the force/moment variation, and (3) synchronously (or frequency) reduce the full matrix to the classical 2×2 matrix in horizontal and vertical direction. Some approaches acquire the steady state solution in step 1 by a steady analysis, such as the Newton-Raphson method. In contrast, this section predicts the steady state solution via numerically integrating the rotor/bearing dynamics and thermodynamics in the time domain to the converged steady state. This follows exactly the same procedure as the ME analysis except that the coefficient solver resets the journal ΔT and thermal bow. The rotor and bearing initial temperature is generally set to be ambient and the rotor position is initially set to be centered in the transient integration to steady state. The rotor mechanical imbalance is also removed for the steady state (time invariant) solution, which uses a convergence criteria that requires the orbit radius $<0.25\%$ of radial bearing clearance at steady state. Thus, comparison with steady state experimental results provides a sound benchmark for the transient ME algorithm utilized herein, albeit the best benchmark will be experimental ME results for gas bearings. The usefulness of the present steady state benchmark is underscored by the fact that no measurement of rotor circumferential temperature or journal ΔT is available for gas FPTPBs. The nonlinear algorithm can simulate the rotor "startup" transients until steady state, so the predicted bearing steady state performance provides a convenient benchmark for the proposed nonlinear transient ME analysis.

Zhu and San Andres [2] measured the steady performance of a hybrid

Table 1
Main parameters of test rig and hybrid gas bearing [2].

Parameter	Value
Rotor mass	0.837 kg, load on pad
Rotor diameter	28.52±0.003 mm
Bearing diameter	28.56±0.003 mm
Diametrical clearance	40±4.5μm
Bearing width	33.2 mm
Pad number and arc length	4 (72°)
Pad pivot offset	60%
Pad Preload	40%
Pad mass moment of inertial	0.253 $g{\cdot}mm^2$
Pad mass	10.85 g
Pad tilting stiffness	20 Nm/rad
Feed orifice diameter	0.38 mm
Supplied gas pressure	2.39 bar (absolute)

FPTPB with 4 pads, and San Andres [20] provided the predictions against the measurements. Table 1 lists their test parameters related to bearing and rotor properties.

The predictions from the TEHD based, proposed gas bearing ME analysis are compared to the steady state predictions [20] and measurements [2] by Zhu and San Andres, by setting the rotor thermal bow in the ME model to zero. The current analysis accurately predicts the trends and values of attitude angle, eccentricity and direct stiffness vs. operating speed provided in Ref. [2], as shown in Fig. 7. Interestingly, the current analysis slightly over predicts the results while San Andres [20] under predicts stiffness relative to their measurements. The differences in predictions may result from differences in some model parameter values. The present TEHD model has parameters with values not provided in Refs. [2,20] and therefore not appearing in Table 1. These include pivot stiffness (5E7 N/m), mixing coefficient (hot air carryover ratio 0.8), heat convection coefficients (200 W/m^{2}K), which are estimated and set to be constant in the simulations. These parameters may vary with test

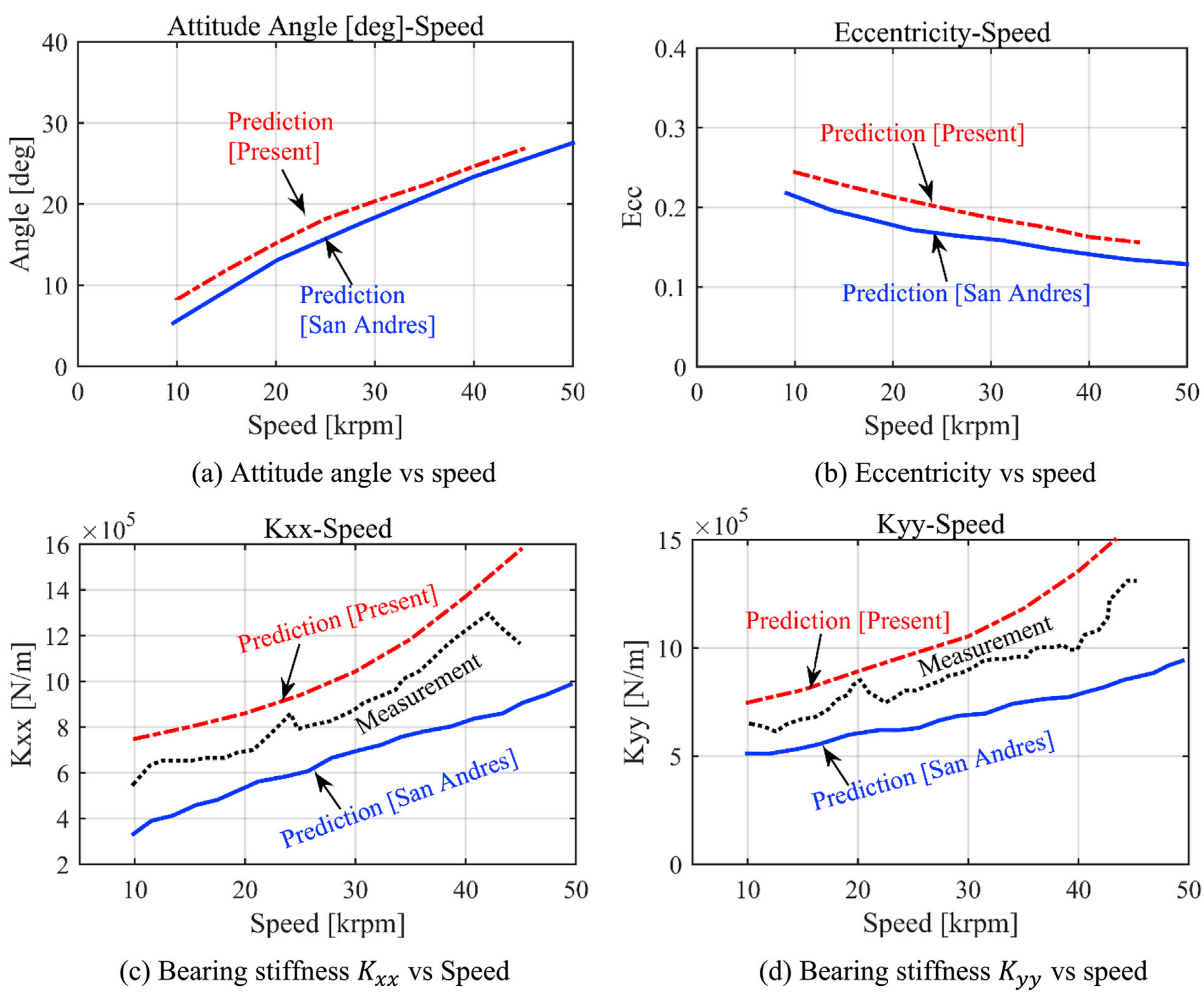

Fig. 7. Comparison of prediction by current method and Ref. [20].

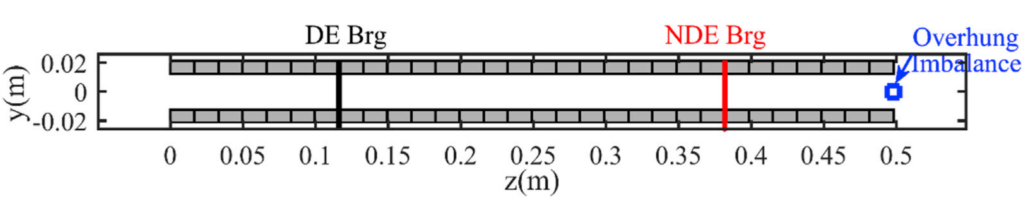

Fig. 8. Rotor geometry for Morton effect model example.

Table 2
Rotor and bearing parameters for the gas bearing Morton effect simulation.

Number of pads	4 (72°)	Pad tilting stiffness	20 N m/rad
Bearing load	29.4 N (LOP)	Pad radial stiffness	5E7 N/m
Pad thickness	3.5 mm	Bearing width	40 mm
Pivot offset	0.6	Radial clearance	27 μm
Preload	0.5	Brg-ambient convection	10 W/(m^{2}K)
Rotor outer/ inner dia.	0.043/ 0.025 m	Ambient/ Reference temp.	25 °C
Rotor length	0.5 m	Overhung mass/ inertia	0.8 kg/2.94 kgm^2
Thermal expansion coeff.	1.2E-5 K^{-1}	Imbalance	1.09E-6 kg m
Heat convection h_{rotor}	200 W/ (m^{2}K)	DE Brg coefficient	$K_{xx} = K_{yy} = 3E6$ N/m; $C_{xx} = C_{yy} = 400$ N/m

operating conditions such as speed, etc. but are treated as constants in the model for sake of simplicity, since the primary focus is on the proposed ME modeling methodology.

5. Example of Morton effect in tilting pad gas bearing

The rotor-gas bearing model to be utilized in the ME instability example is illustrated in Fig. 8, where the two vertical lines indicate the non-drive-end NDE and drive-end DE bearing positions.

The overhung wheel is modeled with lumped translational and rotational inertias at the NDE end of the rotor. The 0.8 kg overhung mass is 21% of the overall rotor mass. The initial mechanical imbalance, resulting from manufacturing or assembly tolerances, is also attached at the rotor NDE. The hollow rotor configuration allows external air to blow through and improve cooling efficiency of the rotor. The ME instability typically occurs only on the overhung end of the rotor, thus only the NDE bearing is analyzed for ME instability, while the DE bearing is modeled simply with its dynamic coefficients. The hydrodynamic model of the NDE ME bearing omits hydrostatic effects, which are assumed to be negligible. The rotor-bearing parameters utilized in the transient ME analysis are listed in Table 2.

5.1. Prediction with and without Morton effect ME

The transient ME analysis is performed while the rotor speed increases linearly from 35 krpm to 41 krpm and then stays constant afterward, as shown in Fig. 9a. The predictions with the ME, i.e., including the rotor thermal bow U_{bow} in Eq. (8), are shown along with the results excluding the ME, i.e., U_{bow} is set to zero. The system is very stable with low vibration, constant phase lag, zero journal ΔT and sufficient film thickness when the ME is excluded, as shown in Fig. 9. Note that all transient results presented in this paper are acquired with the MATLAB numerical integration solver "ODE23" based on a Runge-Kutta method, where the relative tolerance and absolute tolerance are set to be 1E-2 and 1E-3, respectively. The rotor finite element mesh size is $40 \times 7 \times 17$ for both the temperature and the thermal deformation model. The pad mesh size is $15 \times 6 \times 8$ and the gas film mesh is $15 \times 8 \times 8$ for the 3D energy equation solver (all mesh sizes are listed by circumferential, radial and axial direction). With the aforementioned tolerance settings and grids, it took about 5 h to complete the simulation results in Fig. 9 with a PC having 16 GB memory and a 3.4 GHz processor. Convergence analysis has been conducted by doubling the mesh size with smaller tolerances in the numerical solver (1E-3 and 1E-4 for the relative and absolute tolerance, such that the time step will also be smaller), and the predicted rotor and bearing dynamics and temperature were quite close to the presented results).

Effects of including the ME, while operating at a constant speed, are shown to include (1) an oscillation of rotor vibration amplitude and eventual divergence with increasing time, as indicated in Fig. 9b and (2) a continuous increase of the phase lag angle without convergence as indicated in Fig. 9c and (3) an increasing amplitude oscillation of the peak-peak journal ΔT across its circumference, i.e., the temperature difference between the hot spot and cold spot, which eventually exceeds 6°C as indicated in Fig. 9d and (4) a continuously decreasing minimum film thickness inside the gas bearing, leading to rub between the journal and bearing at t = 2.25 min in Fig. 9e and (5) a continuously increasing "effective" thermal imbalance, which is the product of the overhung mass and local thermal bow, which far exceeds the original mechanical imbalance as indicated in Fig. 9f and (6) the occurrence of "spiral" synchronous vibration that can be seen in the 1X polar plot in Fig. 9g, and that clearly indicates that the vibration amplitude and phase angle grow continuously at a constant speed, and (7) the hot spot and cold spot temperatures occurring on the journal surface, at the journal midplane section, are almost 180° apart in Fig. 9h.

The effects on vibration cited above make balancing ineffective in suppressing the ME due to the reliance of balancing on steady amplitudes and phase angles. The above predictions demonstrate that gas FPTPBs may experience the ME instability, similar to oil-lubricated bearings. Neglecting the ME induced thermal bow, may significantly under predict the rotor vibration and miss predicting the synchronous instability at the design stage. Conventional rotordynamic practice seeks to insure that the steady-state imbalance amplitudes are below established limits within the operating speed range. Experience with the ME in oil bearing supported machinery has proven that this practice may be inadequate since the thermal imbalance may become significantly larger than the initial mechanical imbalance. Recall that "thermal imbalance" represents a convenient approximation for the rotor "thermal bow" in Eq. (8) which is the real source that causes spiral vibrations and instability.

5.2. Parametric studies for mechanical imbalance and overhung mass

A natural inclination, especially for those unfamiliar with the ME mechanism, would be to mechanically balance the rotor in response to the presence of high synchronous vibration. The results below confirm that this may prolong the onset time of ME but will be futile in attempting to eliminate the ME. This goal may be reached through changing the amount of overhung mass, as is demonstrated below. Practical implementation of this change is challenging due to the simultaneous performance, cost and size constraints on overhung impellers, couplings, discs, etc. Parametric studies of the imbalance and overhung mass are conducted to investigate the potential influence on ME utilizing the rotor model in section 5.1. The initial mechanical imbalance is reduced to 0.36 g.mm and 0.053 g.mm, i.e., 33% and 5% of the original level. The original level is 1.09 g.mm as shown in Table 2, and for reference produces a centrifugal force of 20 N at 41,000 rpm. In another case, the overhung mass is reduced from 0.8 kg to 0.6 kg. The transient ME analysis at 41 krpm is performed with results shown in Fig. 10, where "Original" illustrates the results with 100% imbalance and 0.8 kg overhung mass, "33% Imb." and "5% Imb." are the transient prediction with reduced imbalance level and 0.8 kg overhung mass, "0.6 kg" indicates the simulations with 100% imbalance level and reduced overhung mass. Reducing the mechanical imbalance from 100% to 33% and 5% does not eliminate the ME instability, as demonstrated in Fig. 10. The rotor vibration amplitude and circumferential ΔT grow slower with smaller imbalance but finally diverge, indicating that the ME induced instability cannot be permanently suppressed through better balancing. This can be intuitively explained from the perspective of thermal imbalance: Initially the thermal imbalance is zero since the rotor is straight, and the synchronous rotor vibration is purely induced by the mechanical imbalance. The rotor circumferential ΔT gradually grows due to the non-uniform film thickness, bending the rotor and causing thermal imbalance. Reducing the initial imbalance slows this process, but finally the thermal imbalance becomes dominant and drives the system unstable as shown in

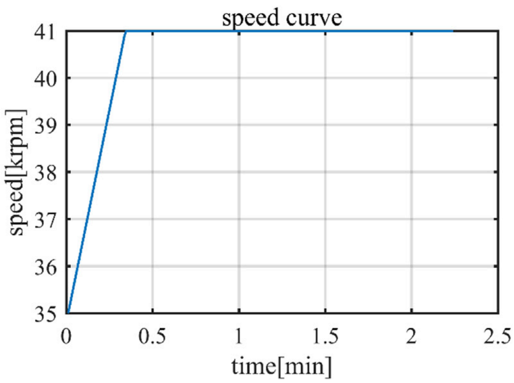

(a) Transient speed curve

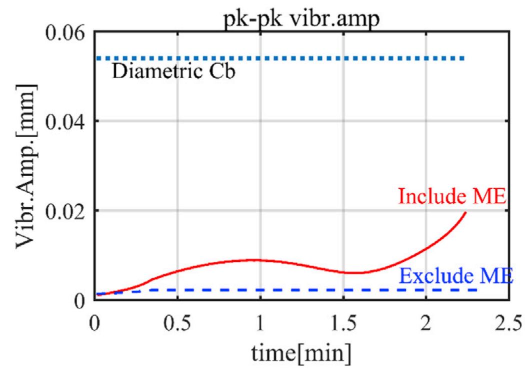

(b) Peak-peak rotor vibration at the bearing

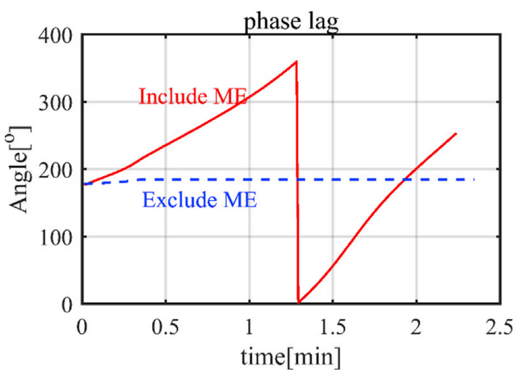

(c) Transient phase of vibration

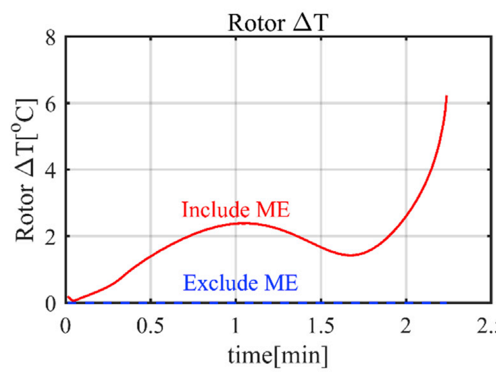

(d) Peak-peak ΔT across journal circumference

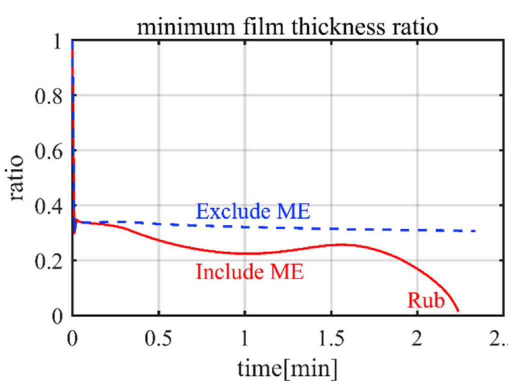

(e) Minimum film thickness ratio

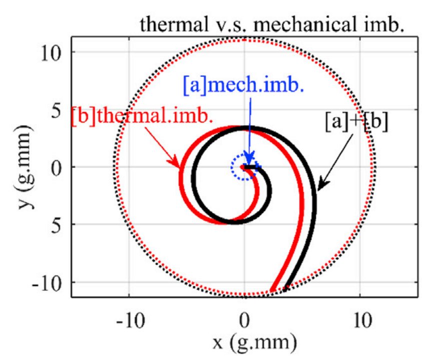

(f) Thermal vs mechanical imbalance

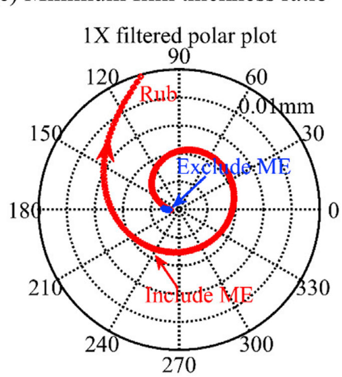

(g) 1X polar plot

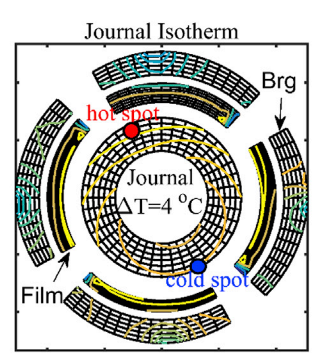

(h) Cross-section isotherms at t=2min, 11s

Fig. 9. Transient prediction at 41 krpm including/excluding ME.

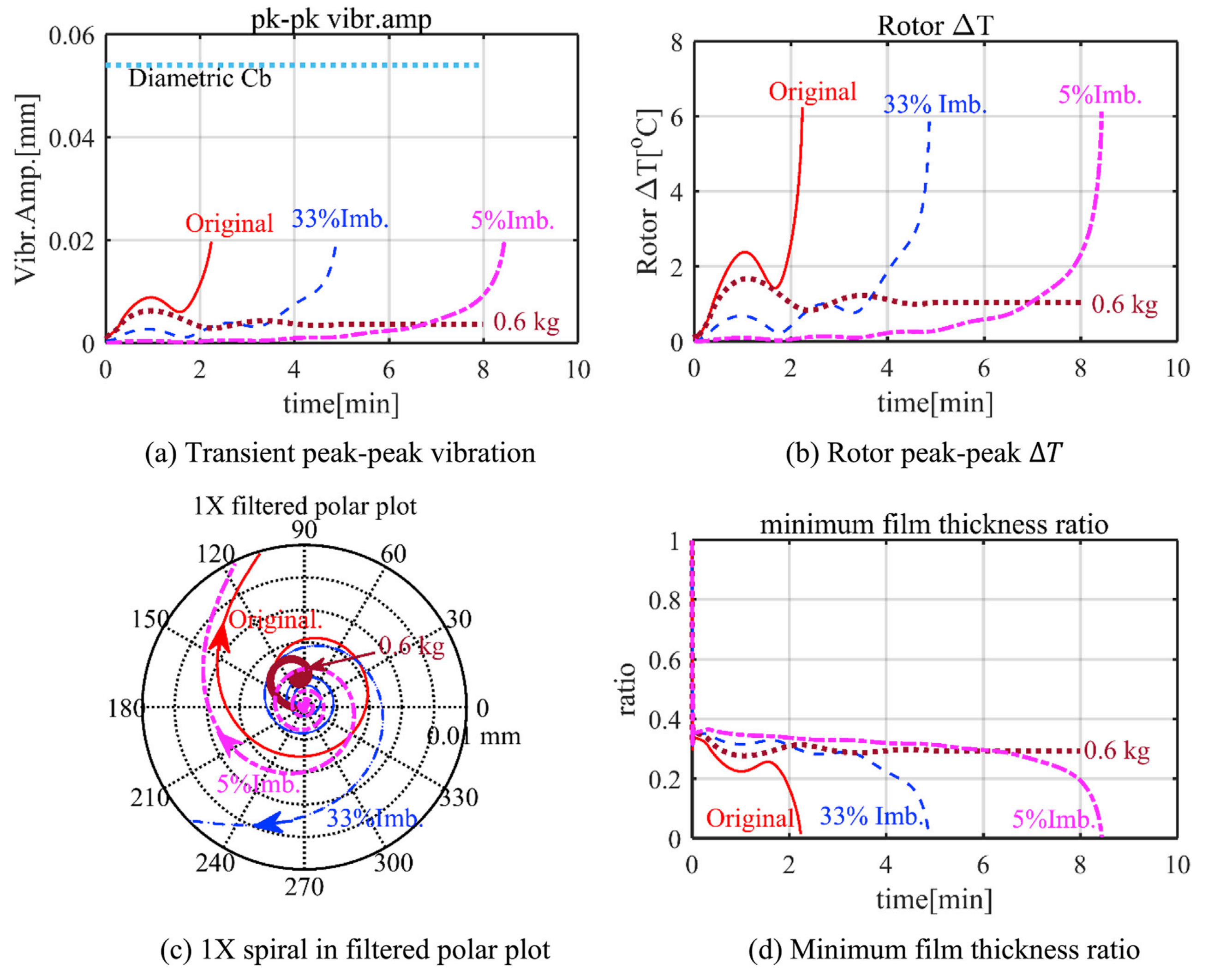

Fig. 10. Transient ME analysis at 41 krpm with various mechanical imbalances and two overhung masses.

Fig. 9f. In contrast, reducing the overhung mass from 0.8 kg to 0.6 kg does permanently eliminate the ME instability. The rotor vibration amplitude at the bearing node, the journal circumferential ΔT and the minimum film thickness of the bearing all converge to steady states, as shown in Fig. 10. The spiral vibrations converge to a point in the 1X polar plot, indicating that the system is stable and the ME instability is permanently eliminated.

6. Discussion and conclusion

The Morton effect ME, i.e., thermally induced synchronous rotordynamic instability, has occurred in widespread applications of rotating machinery utilizing fluid film bearings. The central contribution of the current work is an analytical model, simulation results, and a parametric study for the occurrence of the ME in gas lubricated tilting pad bearings with flexure pivots. Although no industrial or lab case history of ME in tilting pad gas bearings has been reported, the benchmarked, high fidelity, transient TEHD model and predictions provided clearly indicates that the possibility of the ME instability occurring under certain operating conditions and system configurations with gas bearings. The ME prediction methodology presented was verified by comparison with measured gas bearing performance reported in the literature. The rotor configuration considered includes an overhung mass representing an impeller, disc, coupling, etc., which experimentally and analytically been a common feature in oil bearing machinery experiencing the ME. A rotor thermal bow results from the non-uniform circumferential viscous shearing of the bearing gas film, causing a rotor circumferential ΔT and ensuing thermal bending. The 1X polar plot clearly indicates the ME showing the rotor vibration diverging in a spiral shape, with a continuously changing phase lag at constant operating speed. Some important conclusions from this work include:

1. Conventional rotordynamic simulations of steady state imbalance response which exclude the ME, may miss predicting a potentially, machinery operation disabling vibration, even when using gas bearings instead of oil bearings.
2. Rotor phase lag angle changes continuously at constant speed when experiencing the ME, which renders attempts at influence coefficient or modal balancing to be futile. Reducing imbalance level delays the onset of the ME but will not permanently eliminate it.
3. The overhung mass has a critical influence on the ME, and reducing the mass can permanently eliminate it.

Future work includes further verification of the software through both published industrial cases and test rig measurements. One form of benchmarking is to improve the basic capability of matching available results for gas bearings, even in the absence of the ME, i.e. matching stability, critical speed, operating temperatures, etc. The test rig by Tong and Palazzolo [30] for measuring the journal circumferential temperature distribution in the oil bearing system will be retrofitted to measure the same for gas bearings. This rig utilizes 20 RTDs (thermal resistance detectors) embedded slightly beneath the journal surface, and a slip ring to acquire the circumferential temperature of the rotating journal. Moreover, operating conditions will be varied including rotating speeds, mechanical imbalance level, overhung masses (by varying the disks mounted at the rotor NDE). As in Ref. [30] the journal circumferential temperature distribution and the journal orbits, obtained from eddy-current sensors, will be recorded to provide measurements such as the peak-peak ΔT, peak temperature, and the phase angle between the hot spot (with highest temperature) and the high spot (with minimum film thickness) to further benchmark the software.

Acknowledgement

The authors would like to acknowledge funding of this work provided by the Turbomachinery Research Consortium (TRC) (400124-00014) of Texas A&M University.

Appendix. A. Mass flow rate of hydrostatic bearing orifice

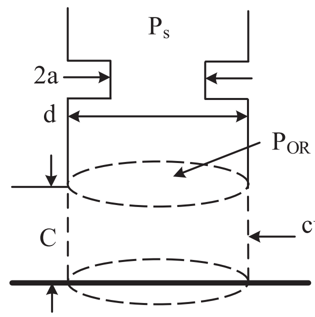

Fig. A. Geometry of feed orifice in gas bearing.

The diagram of the hydrostatic bearing orifice is illustrated in Fig. A, where C is the bearing clearance and d is the feeding hole diameter. The mass flow rate according to Lund [31] is a function of supply pressure P_s and orifice pressure P_{OR}, and can be expressed by Eq. (A), where $\delta = a^2/(dC)$, $\tilde{h} = h/C$.

$$\dot{m}_{OR} = \frac{1}{\sqrt{\mathscr{R}_g T}} \cdot \frac{\pi a^2}{\sqrt{1 + \left(\frac{\delta}{\tilde{h}}\right)^2}} \cdot P_s \cdot m(\overline{P}) \tag{A}$$

Where $m(\overline{P}) = \begin{cases} \sqrt{\frac{2k}{k+1}} \cdot \left(\frac{2}{k+1}\right)^{\frac{1}{k-1}} & \text{for} \quad \overline{P} \le \left(\frac{2}{k+1}\right)^{\frac{k}{k-1}} \\ a\sqrt{\frac{2k}{k-1}} \cdot \overline{P}^{\frac{1}{k}} \cdot \sqrt{1 - \overline{P}^{\frac{k-1}{k}}} & \left(\frac{2}{k+1}\right)^{\frac{k}{k-1}} \le \overline{P} \le 1 \end{cases}$, $\overline{P} = P_{OR}/P_s$, $k = 1.4$, $a = 1$ k is the gas specific heat ratio and a is a nonisentropic loss coefficient.

References

[1] Osborne D, San Andrés L. Comparison of rotordynamic analysis predictions with the test response of simple gas hybrid bearings for oil free turbomachinery. J Eng Gas Turbines Power 2006;128(3):634–43.
[2] Zhu X, San Andrés L. Rotordynamic performance of flexure pivot hydrostatic gas bearings for oil-free turbomachinery. J Eng Gas Turbines Power 2007;129(4):1020–7.
[3] Zeidan F. Developments in fluid film bearing technology. Turbomach Int 1992;(6):33.
[4] Armentrout R, Paquette D. Rotordynamic characteristics of flexure-pivot tilting-pad journal bearings. Tribol Trans 1993;36(3):443–51.
[5] Al-Ghasem A, Childs D. Rotordynamic coefficients measurements versus predictions for a high-speed flexure-pivot tilting-pad bearing (load-between-pad configuration). J Eng Gas Turbines Power 2006;128(4):896–906.
[6] Fillon M, Bligoud J, Frêne J. Experimental study of tilting-pad journal bearings—comparison with theoretical thermoelastohydrodynamic results. ASME Journal of Tribology 1992;114(3):579–87.
[7] Kim J, Palazzolo A, Gadangi R. Dynamic characteristics of TEHD tilt pad journal bearing simulation including multiple mode pad flexibility model. J Vib Acoust 1995;117(1):123–35.
[8] Shi F, Wang Q. A mixed-TEHD model for journal-bearing conformal contacts—Part I: model formulation and approximation of heat transfer considering asperity contact. J Tribol 1998;120(2):198–205.
[9] Keogh P, Morton P. The dynamic nature of rotor thermal bending due to unsteady lubricant shearing within a bearing. Proc R Soc Lond A 1994;445:273–90.
[10] de Jongh F, van der Hoeven P. Application of a heat barrier sleeve to prevent synchronous rotor instability. In: Proceedings of the 27th turbomachinery symposium; 1998.
[11] Suh J, Palazzolo A. Three-dimensional thermohydrodynamic Morton effect simulation—Part I: theoretical model. J Tribol 2014;136(3):031706.
[12] Tong X, Palazzolo A, Suh J. Rotordynamic Morton effect simulation with transient, thermal shaft bow. J Tribol 2016;138(3):031705.
[13] Tong X, Palazzolo A, Suh J. A review of the rotordynamic thermally induced synchronous instability (Morton) effect. Appl Mech Rev 2017;69(6):060801.
[14] Salehi M, Swanson E, Heshmat H. Thermal features of compliant foil bearings-theory and experiments. ASME Journal of Tribology 2001;123(3):566–71.
[15] Howard S, et al. Dynamic stiffness and damping characteristics of a high-temperature air foil journal bearing. Tribol Trans 2001;44(4):657–63.
[16] Radil K, Howard S, Dykas B. The role of radial clearance on the performance of foil air bearings. Tribol Trans 2002;45(4):485–90.
[17] Peng Z, Khonsari M. A thermohydrodynamic analysis of foil journal bearings. J Tribol 2006;128(3):534–41.
[18] Kim T, San Andrés L. Thermohydrodynamic model predictions and performance measurements of bump-type foil bearing for oil-free turboshaft engines in rotorcraft propulsion systems. J Tribol 2010;132(1):011701.
[19] Sim K, Kim D. Thermohydrodynamic analysis of compliant flexure pivot tilting pad gas bearings. J Eng Gas Turbines Power 2008;130(3):032502.
[20] San Andrés L. Hybrid flexure pivot-tilting pad gas bearings: analysis and experimental validation. J Tribol 2006;128(3):551–8.
[21] Lee J, Palazzolo A. Morton effect cyclic vibration amplitude determination for tilt pad bearing supported machinery. J Tribol 2013;135(1):011701.

[22] Young W, Budynas R. In: Roark's formulas for stress and strain, vol. 7. McGraw-Hill New York; 2002.

[23] Tucker P, Keogh P. On the dynamic thermal state in a hydrodynamic bearing with a whirling journal using CFD techniques. J Tribol 1996;118(2):356–63.

[24] Gomiciaga R, Keogh P. Orbit induced journal temperature variation in hydrodynamic bearings. J Tribol 1999;121(1):77–84.

[25] Rindi A, et al. An efficient iterative approach for the analysis of thermal instabilities in rotating machines. J Vib Acoust 2017;139(6):061019.

[26] Balbahadur A, Kirk R. Part I—theoretical model for a synchronous thermal instability operating in overhung rotors. Int J Rotating Mach 2004;10(6):469–75.

[27] Childs D, Saha R. A new, iterative, synchronous-response algorithm for analyzing the Morton effect. J Eng Gas Turbines Power 2012;134(7):072501.

[28] Tong X, Palazzolo A. Double overhung disk and parameter effect on rotordynamic synchronous instability—Morton Effect—Part I: theory and modeling approach. ASME. J. Tribol. 2016;139(1):011705.

[29] API 617. Axial and centrifugal compressors and expander-compressors for petroleum, chemical and gas industry services. seventh ed. Washington, DC: American Petroleum Institute; 2004.

[30] Tong X, Palazzolo A. Measurement and prediction of the journal circumferential temperature distribution for the rotordynamic Morton effect. J Tribol 2018;140(3):031702.

[31] Lund J. A theoretical analysis of whirl instability and pneumatic hammer for a rigid rotor in pressurized gas journal bearings. ASME J. Lubr. Technol 1967;89(2):154–66.